THE EUROPEAN
PHYSICAL JOURNAL D

Regular Article - Clusters and Nanostructures

Microhydration of ionized building blocks of DNA/RNA: infrared spectra of pyrimidine$^+$-(H$_2$O)$_{1-3}$ clusters

Kuntal Chatterjee[1] and Otto Dopfer[1,a]

[1] Institut für Optik und Atomare Physik, Technische Universität Berlin, Hardenbergstr. 36, 10623 Berlin, Germany

Abstract. Hydration of biomolecules is an important physiological process that governs their structure, stability, and function. Herein, we probe the microhydration structure of cationic pyrimidine (Pym), a common building block of DNA/RNA bases, by infrared photodissociation spectroscopy (IRPD) of mass-selected microhydrated clusters, Pym$^+$-W$_n$ (W=H$_2$O), in the size range n = 1–3. The IRPD spectra recorded in the OH and CH stretch range are sensitive to the evolution of the hydration network. Analysis with density functional theory calculations at the dispersion-corrected B3LYP-D3/aug-cc-pVTZ level provides a consistent picture of the most stable structures and their energetic and vibrational properties. The global minima of Pym$^+$-W$_n$ predicted by the calculations are characterized by H-bonded structures, in which the H-bonded W$_n$ solvent cluster is attached to the most acidic C4–H proton of Pym$^+$ via a single CH...O ionic H-bond. These isomers are identified as predominant carrier of the IRPD spectra, although less stable local minima provide minor contributions. In general, the formation of the H-bonded solvent network (exterior ion solvation) is energetically preferred to less stable structures with interior ion solvation because of cooperative nonadditive three-body polarization effects. Progressive hydration activates the C4–H bond, along with increasing charge transfer from Pym$^+$ to W$_n$, although no proton transfer is observed in the size range $n \leqslant 3$. The solvation with protic, dipolar, and hydrophilic W ligands is qualitative different from solvation with aprotic, quadrupolar, and hydrophobic N$_2$ ligands, which strongly prefer interior ion solvation by π stacking interactions. Comparison of Pym$^+$-W with Pym-W and H$^+$Pym-W reveals the drastic effect of ionization and protonation on the Pym...W interaction.

1 Introduction

The structure, stability, and function of almost all biomolecules are strongly governed by their hydration environment, and without hydration these macromolecules often remain inactive [1]. In various cases, the surface water molecules attached to these large biochemical architectures, which are popularly known as biological or interfacial water, are key to their function [2–10]. Such surface water molecules actively participate in charge transport [3,8,10–14] and are crucial for recognition of proteins and drugs through balancing enthalpic and entropic contributions to the overall free energy [15–17].

The molecular picture involving the interaction between these biological water molecules and small building blocks within these large biomolecules often provides information about the function of macromolecules. Mass spectrometry in combination with infrared (IR) spectroscopy and computational chemistry is one of the powerful approaches to probe such interactions at the microscopic level [18–34]. Herein, we apply this combined technique to investigate the microhydration network of the pyrimidine cation (Pym$^+$). The Pym heterocycle is the primary building block of the uracil, thymine, and cytosine nucleobases, which are fundamental constituents of the genetic materials DNA and RNA [35,36]. Furthermore, most biomolecules occur in various charged states (ionized or (de-)protonated) in the physiological medium. These various charged states strongly influence the nature of the intermolecular forces and thus the solvent binding motifs. In this work, we investigate such interactions between Pym$^+$ and neutral solvent molecules, including the effect of solvent polarity on solvent binding motifs and interaction strengths.

In addition to its importance in biophysical phenomena, the Pym···water interaction in its various charged states has substantial significance in the area of molecular astrochemistry. For instance, UV irradiation of pyrimidine: H$_2$O ices results in the formation of nucleobases such as uracil [37–39], which was isolated in different carbonaceous chondrites [40–42]. This is important to understand the enigmatic prebiotic chemistry

that perhaps leads to the beginning of life on planet earth.

We recently reported IR photodissociation (IRPD) spectra of microhydrated structures of protonated Pym, $H^+Pym\text{-}W_{n\leqslant 4}$ (W=H_2O), which confirmed the exclusive N-protonation of neutral Pym and the preference of polar W for forming NH$\cdots$O type linear ionic hydrogen bonds (H-bonds) [43]. The cluster growth through progressive addition of W ligands occurs *via* exterior ion solvation that leads to a growing H-bonded W_n network attached to H^+Pym. Although a recent mass spectrometry study showed bimolecular solute-to-solvent proton transfer at $n = 4$ [44], the IRPD spectra do not show unambiguous evidence for such proton migration up to $n = 4$, in line with computational data [43]. The same study also reported such a proton transfer in the case of ionized $Pym^+\text{-}W_n$ clusters at $n = 4$ and the preference for internal ion solvation over exterior ion solvation [44]. However, the conclusions were based on density functional theory (DFT) calculations at the M06-2X level combined with mass spectrometric experiments. Such a combined approach is not always reliable in the correct prediction of structures, as has been shown recently for the example of microhydrated clusters of the naphthalene cation [31,45,46]. To this end, we investigate herein the $Pym^+\text{-}W_n$ clusters by the much more structure-sensitive IR spectroscopic approach and probe the various ligand binding motifs arising from the increasing number of solvent molecules with the aid of dispersion-corrected DFT calculations at the B3LYP-D3/aug-cc-pVTZ level. Comparison with the previously studied $Pym^+\text{-}(N_2)_n$ clusters using the same spectroscopic and computational approach [47] illustrates the effect of solvent polarity on the interaction potential with respect to both structure (preferred binding sites and solvation network) and binding energy. We also compare our results for $Pym^+\text{-}W$ with the properties of neutral Pym-W [43,48–51] to evaluate the effect of ionization on structure, binding motif, and interaction energy, which is fundamental to comprehend the charge-induced changes arising in solvent binding motifs of biologically relevant molecules.

2 Experimental and theoretical methods

IRPD spectra of size-selected $Pym^+\text{-}L_n$ clusters with L = W ($n = 1$–3) and L = N_2 ($n = 1$–2) are obtained in a quadrupole tandem mass spectrometer coupled to an electron ionization source and an octopole ion guide [19,52]. Briefly, the clusters are produced in a pulsed supersonic plasma expansion by electron and/or chemical ionization of Pym and subsequent clustering reactions in the high-pressure region of the expansion. N_2 carrier gas is passed at a pressure of 8-10 bar through a sample reservoir containing liquid Pym (Sigma-Aldrich, $\geqslant$ 98%, used without further purification, heated to 60°C). To produce hydrated clusters, distilled water is added to the gas line. The desired $Pym^+\text{-}L_n$ par-

ent clusters are mass-selected in the first quadrupole and irradiated in the adjacent octopole with a tunable IR laser pulse (ν_{IR}, 10 Hz, 2–5 mJ, bandwidth $1\,cm^{-1}$) of an optical parametric oscillator pumped by a Q-switched Nd:YAG laser. Calibration of ν_{IR} to better than $1\,cm^{-1}$ is achieved by a wavemeter. Resonant vibrational excitation followed by intracluster vibrational redistribution leads to the loss of a single water or all N_2 ligands. The resulting fragment ions are mass-selected by the second quadrupole and recorded with a Daly detector as a function of ν_{IR} to derive the IRPD spectrum of the parent cluster. The IRPD yield is linearly normalized for laser intensity variations measured with a pyroelectric detector. The contribution of the metastable signal is subtracted from the laser-induced dissociation signal by triggering the ion source at twice the laser repetition rate. The observed peak widths of vibrational transitions are mainly due to unresolved rotational structure, lifetime broadening, sequence hot bands involving inter- and intramolecular modes, and possibly contributions from different structural isomers.

To aid in the analysis of the measured IRPD spectra, conceivable $Pym^+\text{-}L_n$ clusters are computed by using DFT calculation at the B3LYP-D3/aug-cc-pVTZ level [53]. This dispersion-corrected functional accounts well for the electrostatic, induction, and dispersion forces and the IR spectra of the investigated clusters [31,32,54–60]. For example, there is a quantitative agreement between the computed ($D_0 = 1103\,cm^{-1}$) and experimental ($D_0 = 1105 \pm 10\,cm^{-1}$) binding energies of the W_2 dimer [61]. For comparison, neutral Pym, W, and Pym-W are also computed to understand the effect of ionization on their molecular properties. All coordinates are allowed to relax during the search for stationary points, and their nature as minima or transition states are verified by harmonic frequency analysis. For energy optimization, the tight convergence criterion ($< 10^{-6}$ hartree or $< 0.2\,cm^{-1}$) with ultrafine integration grid is employed. Harmonic intramolecular vibrational frequencies are subjected to a linear scaling factor of 0.96221, derived from a comparison of computed CH and OH stretch frequencies of neutral Pym and W with their measured values [62–65]. Scaled harmonic IR stick spectra are convoluted with a Gaussian line shape (fwhm = $10\,cm^{-1}$) for convenient comparison with the experimental spectra. All relative energies (E_e) and equilibrium dissociation energies (D_e) are corrected for harmonic zero-point vibrational energy to derive E_0 and D_0 values. Gibbs free energies (G) are reported for $T = 298.15$ K. If not stated otherwise, the total intermolecular dissociation energies (D_0) are determined with respect to the molecular Pym^+ and W monomer fragments. Previous experience with the employed DFT level demonstrates that basis set superposition errors are less than 1% [31,59], and thus, they are not considered further here. Cartesian coordinates of all relevant structures and their energies are available in the supplementary material. The atomic charge distribution and second-order perturbation energies ($E^{(2)}$) of the donor–acceptor orbital interactions involved in the H-bonds
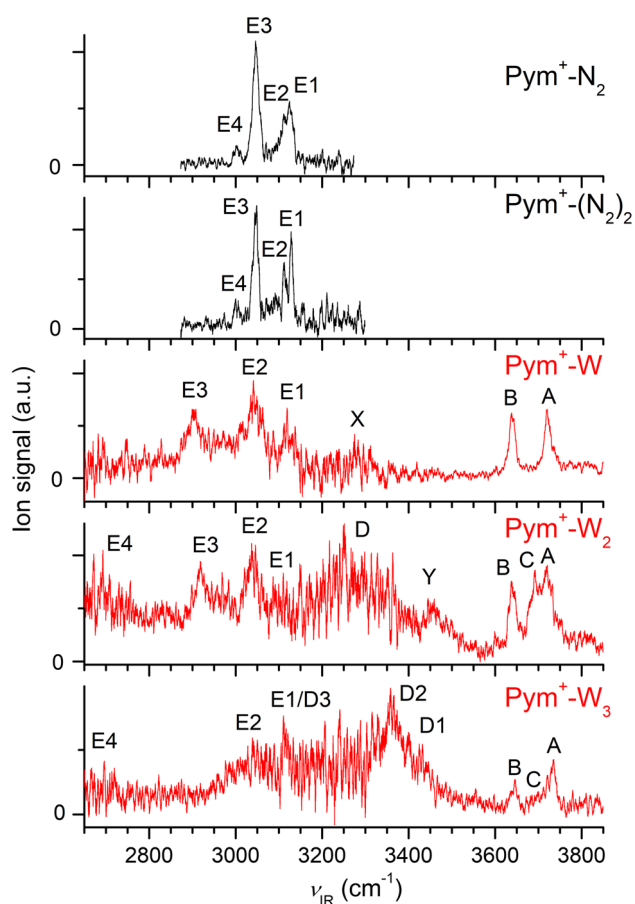
Fig. 1 IRPD spectra of Pym$^+$-L$_n$ clusters with L = W (n = 1–3) and L = N$_2$ (n = 1–2) recorded in the Pym$^+$-W$_{n-1}$ and Pym$^+$ fragment channels for L = W and N$_2$, respectively. The positions, widths, and vibrational and isomer assignments of the transitions observed (A-E) are listed in Table 1

are evaluated using the natural bond orbital (NBO) approach (Figure S1 and S2 in supplementary material) [66]. To further estimate the strength of these H-bonds, noncovalent interaction (NCI) calculations are performed by analyzing the reduced gradient of the electron density, $s(\rho) \sim |grad(\rho)|/\rho^{4/3}$, as a function of electron density ρ oriented by the sign of second eigenvalue λ_2 of the Hessian, $\rho* = \rho sign(\lambda_2)$ [67,68]. The strength of the intermolecular bonds can be estimated by comparing the magnitude of the $-\rho*$ value (Figure S3 in supplementary material).

3 Results and discussion

The IRPD spectra of Pym$^+$-W$_{1-3}$ and Pym$^+$-(N$_2$)$_{1-2}$ acquired between 2650 and 3800 cm^{-1} are displayed in Fig. 1. The positions, widths, and vibrational and isomer assignments of the experimental bands observed (labelled A-F) are listed in Table 1. The measured IR spectral range probes OH and CH stretch fundamentals

($\nu_{OH/CH}$) to identify the contributing isomers, which differ by their ligand binding sites. The free and bound XH stretch modes (X = O/C) are classified as $\nu_{XH}{}^f$ and $\nu_{XH}{}^b$, respectively. Bands A–C occurring in the 3600-3800 cm^{-1} range arise from $\nu_{OH}{}^f$ modes, bands D in the 3100-3500 cm^{-1} range are due to $\nu_{OH}{}^b$ modes, and bands E are attributed to $\nu_{CH}{}^f$ (3000-3200 cm^{-1}) and $\nu_{CH}{}^b$ (2600-3100 cm^{-1}). The strongly size-dependent appearance of the IRPD spectra provides a sensitive probe of the evolution of the solvation structure. As shown in our recent publication [47], the IRPD data of Pym$^+$-(N$_2$)$_{1-2}$ in the CH stretch range unravel the vibrational properties of bare Pym$^+$ and the solvation of Pym$^+$ by quadrupolar N$_2$ ligands. Herein, we focus on the perturbation of the geometric and vibrational properties of Pym$^+$ caused by microhydration and the evolution of the hydration network arising from sequential water addition. To this end, we first briefly review the structural, energetic, and vibrational properties of Pym, Pym$^+$, and Pym$^+$-(N$_2$)$_n$ relevant for the present work, before we discuss microhydrated Pym$^+$-W$_n$ clusters in more detail.

3.1 Pym, Pym$^+$, and W monomers

Both Pym and Pym$^+$ exhibit C_{2v} symmetry in their respective planar $^1A_1$ and $^2B_2$ ground electronic states (S$_0$ and D$_0$), as revealed from electron diffraction and microwave, IR, Raman, and photoelectron spectroscopy [62–64,69–77]. The calculated adiabatic ionization energy (IE) matches reasonably well the experimental value (IE = 73568 vs. 75261 cm^{-1} [64,76, 77]). The excess positive charge mainly resides on the peripheral hydrogens. In line with the shape of the corresponding in-plane HOMO of b$_2$ symmetry [47], ionization elongates the N1–C2 (N3–C2) and N1–C6 (N3–C4) bonds (by 11 and 18 mÅ), while the C4–C5 (C5–C6) bonds contract (by 6 mÅ). In parallel, ionization slightly reduces the C–H bond lengths, which in turn increases the average ν_{CH} frequency ($\Delta\nu_{CH}$ = +74, +27, −1, +2 cm^{-1} for ν_{C2H}, ν_{C5H}, $\nu_{C4H/C6H}$(a), $\nu_{C4H/C6H}$(s)), with a simultaneous enhancement in their IR intensity (Fig. 2). The O–H bond parameters of neutral W in its $^1A_1$ ground state (r_{OH} = 0.9619 Å, $\nu_{3/1}$ = 3752/3653 cm^{-1}) are close to the experimental values (0.9578 Å, 3756/3657 cm^{-1}) [65,78]. The minor discrepancy in the ν_{OH} modes ($\Delta\nu_{OH}$ = −4 cm^{-1}) arises because of the simultaneous consideration of the ν_{CH} modes of Pym and the ν_{OH} modes of W when determining the single scaling factor.

3.2 Pym$^+$-(N$_2$)$_n$

Complexation of Pym$^+$ with quadrupolar N$_2$ ligands occurs either *via* π-bonding or CH…N$_2$ H-bonding [47]. The latter binding motif leads to three possible isomers arising from the three nonequivalent aromatic CH proton donor groups (Fig. 3). The formation of the ionic CH…N$_2$ H-bond elongates the corresponding

Table 1 Positions, widths (fwhm in parentheses), and suggested vibrational and isomer assignments of the transitions observed in the IRPD spectra of Pym^+-L_n clusters (Fig. 1) to the most stable isomers obtained at B3LYP-D3/aug-cc-pVTZ level

	Exp (cm⁻¹)	Calc (cm⁻¹)[a]	Vibration	Isomer
W	3756[b]	3752 (63, b_2)	ν_3	W
	3657[b]	3653 (5, a_1)	ν_1	W
W_2	3746[c]	3743 (84, a'')	ν_3	W_2
	3735[c]	3724 (86, a')	ν_f	W_2
	3654[c]	3648 (10, a')	ν_1	W_2
	3601[c]	3537 (341, a')	ν_{OH}^{b}	W_2
Pym	3074[d]	3076 (9, a_1)	ν_{C5H}	Pym
	3050[d]	3043 (13, a_1)	ν_{C2H}	Pym
	3039[d]	3032 (18, b_2)	$\nu_{C4H/C6H}(as)$	Pym
	3002[d]	3029 (14, a_1)	$\nu_{C4H/C6H}(s)$	Pym
$Pym^{+[e]}$	3124 ± 2	3117 (20, a_1)	ν_{C2H}	Pym^+
	3112 ± 2	3103 (15, a_1)	ν_{C5H}	Pym^+
	3045 ± 2	3031 (49, b_2)	$\nu_{C4H/C6H}(as)$	Pym^+
	3045 ± 2	3031 (13, a_1)	$\nu_{C4H/C6H}(s)$	Pym^+
$Pym^+-N^{[e]}$	E1 3125 (20)	3119 (18, a'), 3117 (18, a')	ν_{C2H}^{f}	π, C4
	E2 3111 (16)	3103 (14, a'), 3103 (15, a')	ν_{C5H}^{f}	π, C4
	E3 3046 (15)	3032 (45, a''), 3032 (29, a')	$\nu_{C4H/C6H}(as)^{f}, \nu_{C6H}^{f}$	π, C4
		3032 (12, a')	$\nu_{C4H/C6H}(s)^{f}$	π
	E4 3001 (20)	3008 (200, a')	ν_{C4H}^{b}	C4
$Pym^+-(N)_2^{[e]}$	E1 3128 (8)	3120 (17, a_1), 3119 (17)	ν_{C2H}^{f}	π/π, C4/π
	E2 3112 (10)	3103 (13, a_1), 3103 (14)	ν_{C5H}^{f}	π/π, C4/π
	E3 3048 (16)	3033 (41, b_2), 3033 (27)	$\nu_{C4H/C6H}(as)^{f}, \nu_{C6H}^{f}$	π/π, C4/π
		3033 (11, a_1)	$\nu_{C4H/C6H}(s)^{f}$	π/π
	E4 3003 (14)	3011 (187)	ν_{C4H}^{b}	C4/π
		3011 (79, a_1), 3010 (301, b_2)	$\nu_{C4H/C6H}(s/a)^{b}$	C4/C6
Pym^+-W	A 3720 (17)	3725 (114, a''), 3720 (106, a'')	ν_3	C4, C4/C5
	B 3638 (18)	3637 (64, a'), 3636 (58, a')	ν_1	C4, C4/C5
	X 3270 (60)[f]		$2\beta_{OH}$	
	E1 3119 (31)	3117 (14, a'), 3118 (13, a')	ν_{C2H}^{f}	C4, C4/C5
		3105 (12, a'), 3111 (25, a')	$\nu_{C5H}^{f}, \nu_{C5H}^{b}$	C4, C4/C5
	E2 3040 (55)	3033 (23, a'), 3032 (24, a')	ν_{C6H}^{f}	C4, C4/C5
	E3 2900 (110)	2842 (848, a'), 2998 (188, a')	ν_{C4H}^{b}	C4, C4/C5
Pym^+-W_2	A 3721 (24)	3736 (113)	ν_3	C4
		3729 (112, a''), 3724 (98, a'')	ν_3	C4–C5/C6
	C 3693 (26)	3695 (125)	ν_f	C4
	B 3637 (21)	3646 (30)	ν_1	C4
		3641 (49, a'), 3638 (48, a')	ν_1	C4–C5/C6
	Y 3450 (42)[f]		$\nu_{OH}^{b} + \nu_s$	
	D 3250 (190)	3336 (1321)	ν_{OH}^{b}	C4
	E1 3111 (55)	3117 (8), 3106 (8)	$\nu_{C2H}^{f}, \nu_{C5H}^{f}$	C4
		3118 (8, a'), 3114 (22, a')	$\nu_{C2H}^{f}, \nu_{C5H}^{b}$	C4–C5/C6
	E2 3036 (37)	3034 (20)	ν_{C6H}^{f}	C4
	E3 2918 (70)	3011 (139, a')	ν_{C6H}^{b}	C4–C5/C6
	E4 < 2800	2652 (1731)	ν_{C4H}^{b}	C4
		2864 (755, a')	ν_{C4H}^{b}	C4–C5/C6
Pym^+-W_3	A 3734 (20)	3738 (210, a'), 3737 (7, a'')	ν_3	C4-b
		3744 (110)	ν_3	C4-l
	C 3700 (30)	3711 (91), 3689 (160)	ν_f	C4-l
	B 3646 (15)	3647 (43, a'), 3647 (17, a'')	ν_1	C4-b
		3652 (24)	ν_1	C4-l
	D1 3425 (75)	3393 (1180, a'')	$\nu_{OH}^{b}(as)$	C4-b
		3390 (708)	ν_{OH}^{b}	C4-l
	D2 3358 (100)	3321 (2362, a')	$\nu_{OH}^{b}(s)$	C4-b
	E1/D3 3110 (47)	3115 (11, a'), 3107 (5)	$\nu_{C2H}^{f}, \nu_{C5H}^{f}$	C4-b

Table 1 continued

Exp (cm^{-1})	Calc $(cm^{-1})^a$	Vibration	Isomer
	3124 (2242)	$\nu_{OH}{}^b$	C4-l
	3115 (181), 3106 (7)	$\nu_{C2H}{}^f$, $\nu_{C5H}{}^f$	C4-l
E2 3040 (60)	3035 (16, a′)	$\nu_{C6H}{}^f$	C4-b
	3035 (18)	$\nu_{C6H}{}^f$	C4-l
E4 < 2750	2316 (2062, a′)	$\nu_{C4H}{}^b$	C4-b
	2517 (2034)	$\nu_{C4H}{}^b$	C4-l

[a] Vibrational symmetry species and IR intensities (in km/mol) are listed in parentheses. [b] Ref. [65], [c] Ref. [92–94], [d] Ref. [62,63], [e] Ref. [43]. [f] The interpretation of these bands is unclear and possible assignments to the overtone of the OH bend of the W ligand (band X, $n = 1$) and the combination band of $\nu_{OH}{}^b$ with the intermolecular OH$\cdots$O stretch mode (ν_s) for band Y ($n = 2$) are tentative
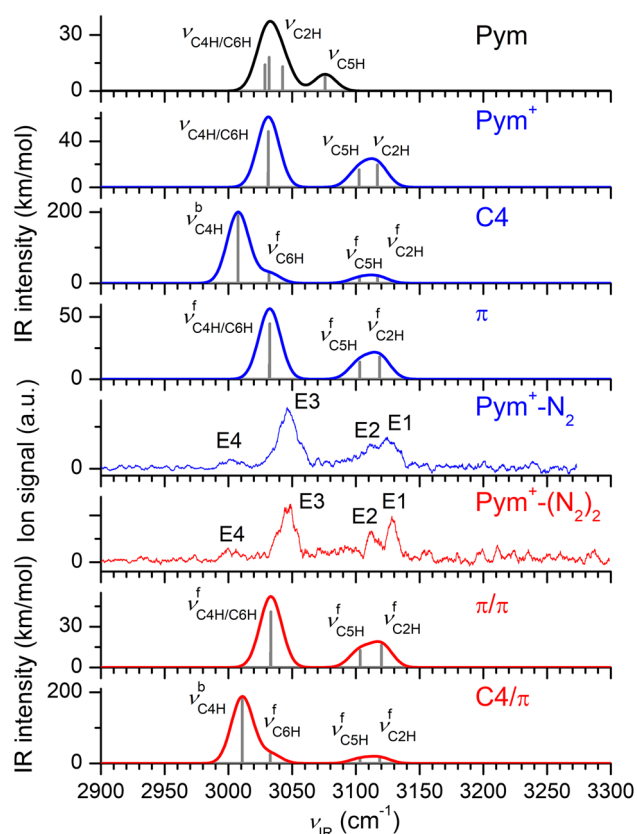
Fig. 2 Comparison of IRPD spectra of Pym$^+$-(N$_2$)$_{1-2}$ with linear IR absorption spectra of Pym, Pym$^+$, and various Pym$^+$-(N$_2$)$_{1-2}$ isomers obtained at the B3LYP-D3/aug-cc-pVTZ level (Table 1, [47])
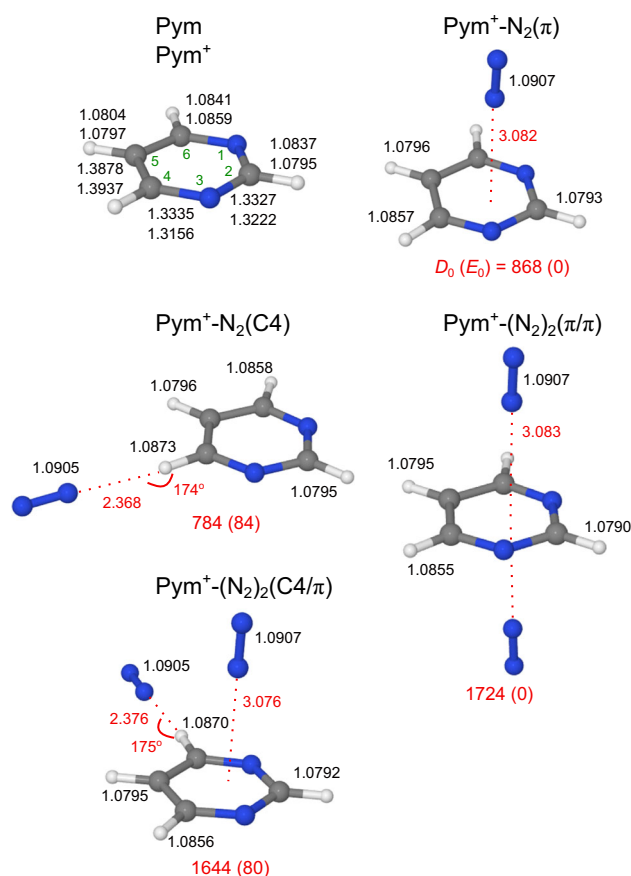

Fig. 3 Optimized geometries of Pym, Pym$^+$ (along with atom numbering), and the most stable Pym$^+$-(N$_2$)$_n$ isomers calculated at the B3LYP-D3/aug-cc-pVTZ level [47]. Binding energies (D_0) and bond lengths are given in cm^{-1} and Å, respectively. Numbers in parentheses correspond to relative energies in cm^{-1} (E_0)

C–H donor bond (~ 1 mÅ), and the effect is largest for the Pym$^+$-N$_2$(C4) isomer, consistent with the most acidic nature of the C4H group, as visible in the longest C–H bond and highest atomic charge on the proton (0.275 e) in bare Pym$^+$. Consequently, this isomer has the highest D_0 value as compared to the other H-bonded isomers ($D_0 = 784$ vs. 775 and 690 cm^{-1} for the C4, C2, and C5 isomers, respectively). However, this value is smaller than the binding energy of the π-bonded Pym$^+$-N$_2$(π) cluster ($D_0 = 868$ cm^{-1}), exhibiting substantial charge-quadrupole,

charge-induced dipole, and dispersion interactions. As expected, π complexation barely affects the geometry of Pym$^+$ ($\Delta r_{CH} \leqslant 0.2$ mÅ), and thus, the ν_{CH} frequencies remain comparable to those of the bare cation ($\Delta \nu_{CH} \leqslant 2$ cm^{-1}, Table 1).

Both the transitions at 3125 (E1), 3111 (E2), and 3046 (E3) cm^{-1} and their relative intensities in the

measured Pym^+-N_2 spectrum agree well with the predicted Pym^+-$N_2(\pi)$ spectrum (Fig. 2), which confirms the dominant contribution of this global minimum, consistent with the thermochemical prediction. A similar agreement is not observed for the H-bonded Pym^+-$N_2(C5)$ and Pym^+-$N_2(C2)$ heterodimers, particularly for their $\nu_{C2H/C5H}{}^b$ modes near $3100\,cm^{-1}$, which confirms their absence (or their very low concentration below the detection limit) [47]. The weak feature E4 at $3001\,cm^{-1}$ is assigned to the $\nu_{C4H}{}^b$ mode of the Pym^+-$N_2(C4)$ isomer calculated at $3008\,cm^{-1}$. Although the remaining ν_{CH} modes of this local minimum overlap with the E1, E2, and E3 bands of the π isomer, the poor experimental IR intensity of the characteristic $\nu_{C4H}{}^b$ mode indicates its small abundance in our ion source. Our qualitative analysis estimates a population ratio of 24:1 for the π and C4 isomers [47].

Addition of the second N_2 ligand to Pym^+-$N_2(\pi)$ preferably occurs at the opposite side of the aromatic ring *via* interior ion solvation, as reflected by the largest D_0 value of the Pym^+-$(N_2)_2(\pi/\pi)$ trimer, $1724\,cm^{-1}$ (Fig. 3). Similar to the dimer case, π complexation barely influences the geometrical and vibrational properties. The experimental bands at 3128 (E1), 3112 (E2), and 3048 (E3) cm^{-1} are again consistent with the corresponding predicted ν_{CH} modes of Pym^+-$(N_2)_2(\pi/\pi)$, and the slight blue shift ($\Delta\nu_{CH} \leqslant 3\,cm^{-1}$) originates from minor noncooperative (i.e., anticooperative) effects by the addition of the second π-bonded N_2 ligand (Fig. 2, Table 1). The almost unshifted weak feature E4 at $3003\,cm^{-1}$ is attributed to the $(C4/\pi)$ and $(C4/C6)$ isomers of Pym^+-$(N_2)_2$ with $D_0 = 1644$ and $1546\,cm^{-1}$. The weak experimental intensity demonstrates the small concentration of these less stable local minima ($< 5\%$) as compared to the most stable (π/π) global minimum. From these π-bonded Pym^+-$(N_2)_n$ clusters, we extrapolate the ν_{CH} frequencies of bare Pym^+ as 3124 ± 2 (ν_{C2H}), 3112 ± 2 (ν_{C5H}), 3045 ± 2 ($\nu_{C4H/6H}(s)$), and $3045 \pm 2\,cm^{-1}$ ($\nu_{C4H/6H}(as)$) [47].

3.3 Pym^+-W

Our extensive search on the potential energy surface of monohydrated Pym^+ yields the five different Pym^+-W isomers shown in Fig. 4, and their IR spectra are compared in Fig. 5. All isomers have a charge-dipole configuration in which the O atom of W approaches the positive charge of Pym^+. Unlike the Pym^+-N_2 dimer, for which π complexation is preferred over CH...L H-bonding, the additional strong charge-dipole and donor–acceptor orbital interactions in Pym^+-W favor ionic H-bonding between the Pym^+ cation and dipolar W. Consequently, the D_0 values of the four H-bonded Pym^+-W dimers are higher than the that of Pym^+-W(π) by at least $350\,cm^{-1}$. Among the H-bonded isomers, the Pym^+-W(C4) global minimum with a C4H...O H-bond has the largest D_0 value ($D_0 = 3597\,cm^{-1}$), which is consistent with the highest acidity of the C4H proton donor group. The single
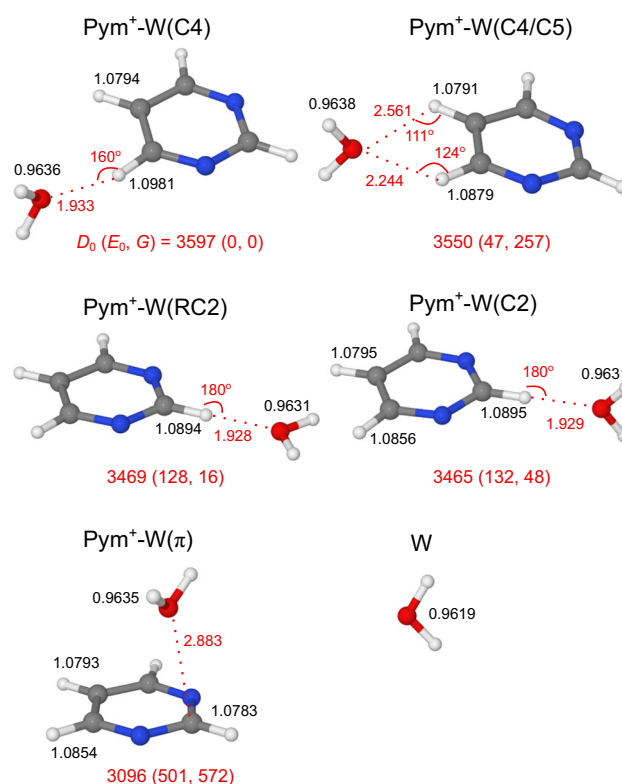

Fig. 4 Optimized structures of various monohydrated Pym^+-W isomers calculated at the B3LYP-D3/aug-cc-pVTZ level. Binding energies (D_0) and bond lengths are given in cm^{-1} and Å, respectively. Numbers in parentheses correspond to relative energies and free energies in cm^{-1} (E_0, G). For comparison, the structure of W is also provided

but rather nonlinear H-bond in this most stable isomer ($\theta_{CHO} = 160°$) with trans configuration suggests that the interaction of one of the two lone pairs of O with the acidic CH group supports the charge-dipole attraction. The CH...O H-bond leads to a significant lengthening of the proton donor bond ($\Delta r_{CH} = 12.2\,m\text{Å}$) and a substantial redshift in the corresponding bound CH stretch frequency ($\nu_{C4H}{}^{(b)} = 2842$ vs. $3045\,cm^{-1}$) with a simultaneous increase in IR intensity ($I_{C4H} = 848$ vs. 49 km/mol) as compared to the bare cation (Fig. 5). Unlike the Pym^+ monomer, this H-bonded $\nu_{C4H}{}^b$ is no longer coupled with the ν_{C6H} mode. This strong hydration-induced perturbation is in line with the NBO and NCI data, which are substantially larger than the corresponding Pym^+-$N_2(C4)$ parameters ($E^{(2)} = 40$ vs. 11.8 kJ/mol, $-\rho* = 0.027$ vs. 0.011 a.u.). The remaining free ν_{CH} modes are nearly unperturbed by monohydration. The computed $\nu_{1/3}$ modes of W are slightly redshifted as compared to bare W ($-\Delta\nu_{1/3} = 16/27\,cm^{-1}$) because of the hydration-induced charge transfer from Pym^+ to W ($q = 35\,me$). The latter also enhances their IR oscillator strength, with a substantial effect particularly on the ν_1 mode (factor 13 for ν_1, factor 2 for ν_3).
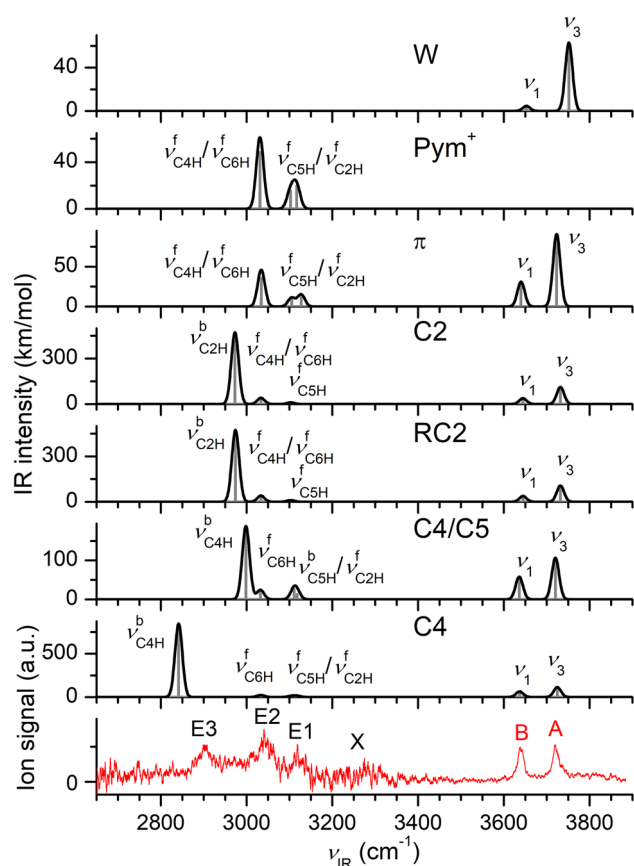
Fig. 5 Comparison of IRPD spectrum of Pym$^+$-W with linear IR spectra of W, Pym$^+$, and Pym$^+$-W isomers (Fig. 4) calculated at the B3LYP-D3/aug-cc-pVTZ level (Table 1)

In the next stable Pym$^+$-W(C4/C5) dimer with $D_0 = 3550\,\mathrm{cm}^{-1}$, W participates in an asymmetric bifurcated H-bond with the C4H and C5H proton donors. This bifurcated H-bond is less strong as compared to the single H-bond in the most stable Pym$^+$-W(C4) dimer, as reflected from the larger average H-bond length and stronger deviation from linearity ($R_{\mathrm{CH\cdots O}} = 2.403$ vs. $1.933\,\text{Å}$, $\theta_{\mathrm{CHO}} = 111°$ and $124°$ vs. $160°$), leading to its slightly lower D_0 value ($E_0 = 47\,\mathrm{cm}^{-1}$). Because of the weaker interaction, the C4H group is less perturbed than in Pym$^+$-W(C4). This result is visible in the slight C4–H bond elongation and the smaller redshift of the corresponding $\nu_{\mathrm{C4H}}{}^{\mathrm{b}}$ mode with respect to the bare Pym$^+$ ($\Delta r_{\mathrm{CH}} = 2\,\mathrm{m\text{Å}}$, $\nu_{\mathrm{C4H}}{}^{(\mathrm{b})} = 2998$ vs. $3045\,\mathrm{cm}^{-1}$). In fact, the C4–H bond is more perturbed than the C5-H bond in Pym$^+$-W(C4/C5), which is evident from the larger H-bond angle and shorter $R_{\mathrm{CH\cdots O}}$ bond distance. Our NBO and NCI data further support this view ($E^{(2)} = 8.3$ vs. $1.5\,\mathrm{kJ/mol}$, $-\rho* = 0.015$ vs. $0.008\,\mathrm{a.u.}$). In addition, the overall charge transfer from Pym$^+$ to W is smaller than for the C4 isomer, suggesting a reduction in binding force ($q = 16$ vs. $35\,m e$). Interestingly, the predicted frequency of the other bound CH mode is slightly

blueshifted from that of Pym$^+$ ($\Delta\nu_{\mathrm{C5H}}{}^{(\mathrm{b})} = 8\,\mathrm{cm}^{-1}$). Surprisingly, a Pym$^+$-W(C5) isomer of Pym$^+$-W with a single CH...O H-bond (similar to the C4 isomer) is not stable and converges to the C4/C5 minimum.

In the two other H-bonded monohydrates, Pym$^+$-W(C2) and Pym$^+$-W(RC2), W forms a linear H-bond with the C2H proton donor group. In the C2 isomer, the two O–H bonds lie perpendicular to the ring plane, while they are coplanar with the aromatic ring in the RC2 isomer, leading to two structures with $C_{2\mathrm{v}}$ symmetry. Their rather small energy difference of $6\,\mathrm{cm}^{-1}$ indicates that the barrier for internal W rotation around the C_2 axis is rather small. This is in contrast to the C4 isomer, for which steric hindrance with the nearby CH5 proton causes a larger anisotropy in the potential for internal W rotation, with a barrier of $V_{\mathrm{b}} = 117\,\mathrm{cm}^{-1}$ at the planar transition state (Figure S4 in supplementary material). The smallest D_0 values for the C2/RC2 isomers amongst the H-bonded Pym$^+$-W minima result from the weakest acidity of the C2H proton donor group ($D_0 = 3465$ and $3469\,\mathrm{cm}^{-1}$ for C2 and RC2), which is seen from the shortest r_{CH} bond in bare Pym$^+$ ($r_{\mathrm{C2H}} = 1.0795\,\text{Å}$). Although the NBO data only reflect a minor difference from the most stable C4 isomer ($E^{(2)} = 42.5$ and 42.4 vs. $40\,\mathrm{kJ/mol}$), the degree of charge transfer and the NCI values explain the smaller D_0 values of these two isomers ($q = 25$ vs. $35\,m e$, $-\rho* = 0.0266$ and 0.0267 vs. $0.0272\,\mathrm{a.u}$). As a result, the elongation of the proton donor C–H-bonds is smaller as compared to Pym$^+$-W(C4) ($\Delta r_{\mathrm{CH}} = 10$ vs. $12.2\,\mathrm{m\text{Å}}$), illustrating the weakest H-bond in these two C2/RC2 isomers. The smaller redshifts of the ν_{C2H} mode in the C2/RC2 isomers ($\nu_{\mathrm{C2H}}{}^{(\mathrm{b})} = 2973/2974$ vs. $3117\,\mathrm{cm}^{-1}$) compared to that of $\nu_{\mathrm{C4H}}{}^{\mathrm{b}}$ of the C4 isomer confirms this view ($-\Delta\nu_{\mathrm{C2/4H}}{}^{\mathrm{b}} = 144$ and 143 vs. $203\,\mathrm{cm}^{-1}$). Analogous to the other isomers, the free CH stretch modes in the C2/RC2 isomers remain almost unshifted upon monohydration.

The least stable Pym$^+$-W(π) isomer with $D_0 = 1096\,\mathrm{cm}^{-1}$ and W located above the ring has the shortest contact to C2 ($R_{\mathrm{C2O}} = 2.883\,\text{Å}$), because this atom carries the highest positive partial charge of all heavy atoms of the heterocyclic aromatic ring ($q_{\mathrm{C2}} = +0.28\,e$). As observed for the N$_2$ ligand, π hydration barely affects the geometry of Pym$^+$ ($\Delta r_{\mathrm{CH}} \leqslant -1.2\,\text{Å}$), and thus, the free ν_{CH} frequencies and their IR intensities remain close to those of the bare cation ($\Delta\nu_{\mathrm{CH}} \leqslant 11\,\mathrm{cm}^{-1}$, Fig. 5). Because of the weakest bond, charge transfer from Pym$^+$ to W is smallest in Pym$^+$-W(π) ($8\,m e$).

The IRPD spectrum of Pym$^+$-W is compared in Fig. 5 (Table 1) to predicted linear IR absorption spectra of the optimized Pym$^+$-W isomers shown in Fig. 4. For convenience, the spectra predicted for Pym$^+$ and W are also included. The IRPD spectrum features two relatively sharp high-frequency transitions A and B in the free OH stretch range at 3720 and $3638\,\mathrm{cm}^{-1}$, respectively, and several lower-frequency bands in the CH stretch range at 2900 (E3), 3040 (E2), 3119 (E1),

and 3270 (X) cm^{-1}. The predicted $\nu_{1/3}$ modes of W, which are computed at similar spectral positions for all optimized isomers (to within 12 cm^{-1}), are assigned to the bands B and A. Thus, it is difficult to identify the contributing isomers from the OH stretch bands. The derived $\Delta\nu_{1/3}$ redshifts of 19 and 36 cm^{-1} are characteristic for cation-W clusters [46, 79–82]. The broader lowest-frequency band E3 is readily assigned to the $\nu_{C4H}{}^{b}$ mode of the most stable Pym^{+}-W(C4) isomer calculated at 2842 cm^{-1} and a clear-cut spectroscopic signature for the presence of this isomer. The difference of 58 cm^{-1} between measured and predicted frequencies may arise from the strong anharmonic nature of this H-bonded mode or from insufficient description of the harmonic force field at the chosen DFT level. The nonvanishing signal toward the blue end of this band is attributed to the sequence hot band transitions involving intermolecular modes, $\nu_{C4H}{}^{b} + \nu_{x} \leftarrow \nu_{x}$ [55, 79, 83–85]. The E2 and E1 bands match with the free $\nu_{C6H}{}^{f}$ and $\nu_{C5H}{}^{f}/\nu_{C2H}{}^{f}$ modes of this isomer predicted at 3033 and 3105/3117 cm^{-1}, respectively. We assign part of the large intensity of the E2 band to the sequence hot bands associated with $\nu_{C4H}{}^{b}$, although this contribution cannot fully account for the observed intensity. Hence, we suggest that the bound $\nu_{C4H}{}^{b}$ mode of Pym^{+}-W(C4/C5) at 2998 cm^{-1} also contributes to the E2 band, which increases its transition intensity and width. The predicted free $\nu_{C6H}{}^{f}$ and $\nu_{C5H}{}^{f}/\nu_{C2H}{}^{f}$ modes of this bifurcated isomer overlap with the E2 and E1 bands. Although the free CH stretch modes of the C2/RC2 isomers also agree with the E2 and E1 bands, intense characteristic $\nu_{C2H}{}^{b}$ band lies outside the transition width of band E2. Nonetheless, a smaller contribution of both isomers may be evident from the nonvanishing signal at the red side of band E2. A significant contribution of the π isomer to the IRPD spectrum is also excluded because of its high relative energy and the low IR oscillator strengths of its free CH stretch bands. Therefore, the experimental spectrum is mainly attributed to the predominant Pym^{+}-W(C4) isomer along with a significant contribution of the C4/C5 dimer, which is consistent with their thermochemical data ($E_0 = 0$ and 47 cm^{-1}).

3.4 Pym^{+}-W$_2$

The second W ligand binds to the monohydrated cluster either through interior ion solvation by separately interacting with the Pym^{+} core or through exterior ion solvation by extending the solvent network via OH...O H-bonding to the first W ligand, resulting in the eight Pym^{+}-W$_2$ isomers shown in Fig. 6. In analogy to the $n = 1$ case, in the most stable Pym^{+}-W$_2$(C4) dihydrate the H-bonded W$_2$ dimer binds to the most acidic C4H proton donor group. As a result of strong cooperativity of the formation of the H-bonded solvent network, mainly due to nonadditive three-body polarization forces, the total binding energy of $D_0 = 6894$ cm^{-1} exceeds the sum of the individual H-bond energies of Pym^{+}-W(C4) and W$_2$, $D_0 = 3597 + 1103 = 4700$ cm^{-1},

by 2194 cm^{-1} or 47%. This large cooperative effect arising from the second W ligand strengthens the CH...O H-bond, which is evident from the reduced $R_{CH...O}$ bond length and elongated C4–H bond as compared to the Pym^{+}-W(C4) monohydrate ($R_{CH...O} = 1.804$ vs. 1.933 Å, $r_{CH} = 1.1111$ vs. 1.0981 Å). The stronger CH...O ionic H-bond causes a substantially larger redshift of the $\nu_{C4H}{}^{b}$ mode with a simultaneous enhancement of the IR oscillator strength ($-\Delta\nu_{C4H} = 379$ vs. 190 cm^{-1}, $I_{CH} = 1731$ vs. 848 km/mol). Such a substantial solvent-induced perturbation is consistent with the enhanced proton affinity of W$_2$ as compared to W (PA = 808 vs. 691 kJ/mol [86,87]) and is further supported by the increased NBO and NCI values associated with the CH...O H-bond as compared to the $n = 1$ cluster ($E^{(2)} = 65.7$ vs. 40 kJ/mol, $-\rho* = 0.038$ vs. 0.027 a.u.) together with the increased cation-to-solvent charge transfer ($q = 75$ vs. 35 me). The cooperative effect is also visible in the OH...O H-bond, which becomes substantially stronger and shorter than in bare W$_2$ by the presence of the nearby positive Pym^{+} charge and the resulting polarization effects ($R_{OH...O} = 1.768$ vs. 1.947 Å, $r_{OH} = 0.9810$ vs. 0.9696 Å, $D_0 = 3297$ vs. 1103 cm^{-1}, $\nu_{OH}{}^{b} = 3336$ vs. 3537 cm^{-1}, $E^{(2)} = 61$ vs. 32 kJ/mol, $-\rho* = 0.037$ vs. 0.026 a.u.). The remaining free CH modes are largely unperturbed. In addition to the calculated $\nu_{1/3}$ modes of the terminal single-acceptor W ligand (3646/3736 cm^{-1}), the computed spectrum features two additional bands in the OH stretch range resulting from the H-bonded $\nu_{OH}{}^{b}$ mode and dangling free ν_{f} mode at 3336 and 3695 cm^{-1}, respectively, associated with the single-donor single-acceptor W ligand. These latter frequencies are consistent with the respective O–H bond lengths ($r_{OH} = 0.9810$ vs. 0.9626 Å). The computed $\nu_{1/3}$ modes are slightly blueshifted with respect to the corresponding $n = 1$ frequencies ($\Delta\nu_{1/3} = 9/11$ cm^{-1}) due to the increased distance from the positive charge.

The next stable Pym^{+}-W$_2$(C4–C5/C6) isomer with $E_0 = 100$ cm^{-1} exhibits interior ion solvation, with two W ligands forming individual H-bonds to Pym^{+}: a more or less linear one to C4H and a bifurcated one to C5H and C6H. Interestingly, all efforts to optimize a C_{2v} symmetric structure (with either two equivalent linear or two equivalent bifurcated H-bonds) fail and converge to the C_s symmetric C4–C5/C6 structure. As a consequence of the anticooperativity of interior ion solvation, mainly due to nonadditive three-body induction forces and increased charge delocalization, the total binding energy of $D_0 = 6794$ cm^{-1} is lower than twice the sum of the individual H-bond energies of Pym^{+}-W(C4), $D_0 = 2 \times 3597 = 7194$ cm^{-1}, by 400 cm^{-1} or 5.6%. This anticooperative three-body force induced by adding the second W reduces the H-bond strength of the nearly linear C4H...O bond as compared to its $n = 1$ counterpart, as illustrated by the slightly longer $R_{CH...O}$ distance and the reduced C4–H bond length ($R_{CH...O} = 1.953$ vs. 1.933 Å, $r_{CH} = 1.0965$ vs. 1.0981 Å). Consequently, the $\nu_{C4H}{}^{b}$ mode is slightly less redshifted compared to the C4 monohydrate ($-\Delta\nu_{C4H} =$
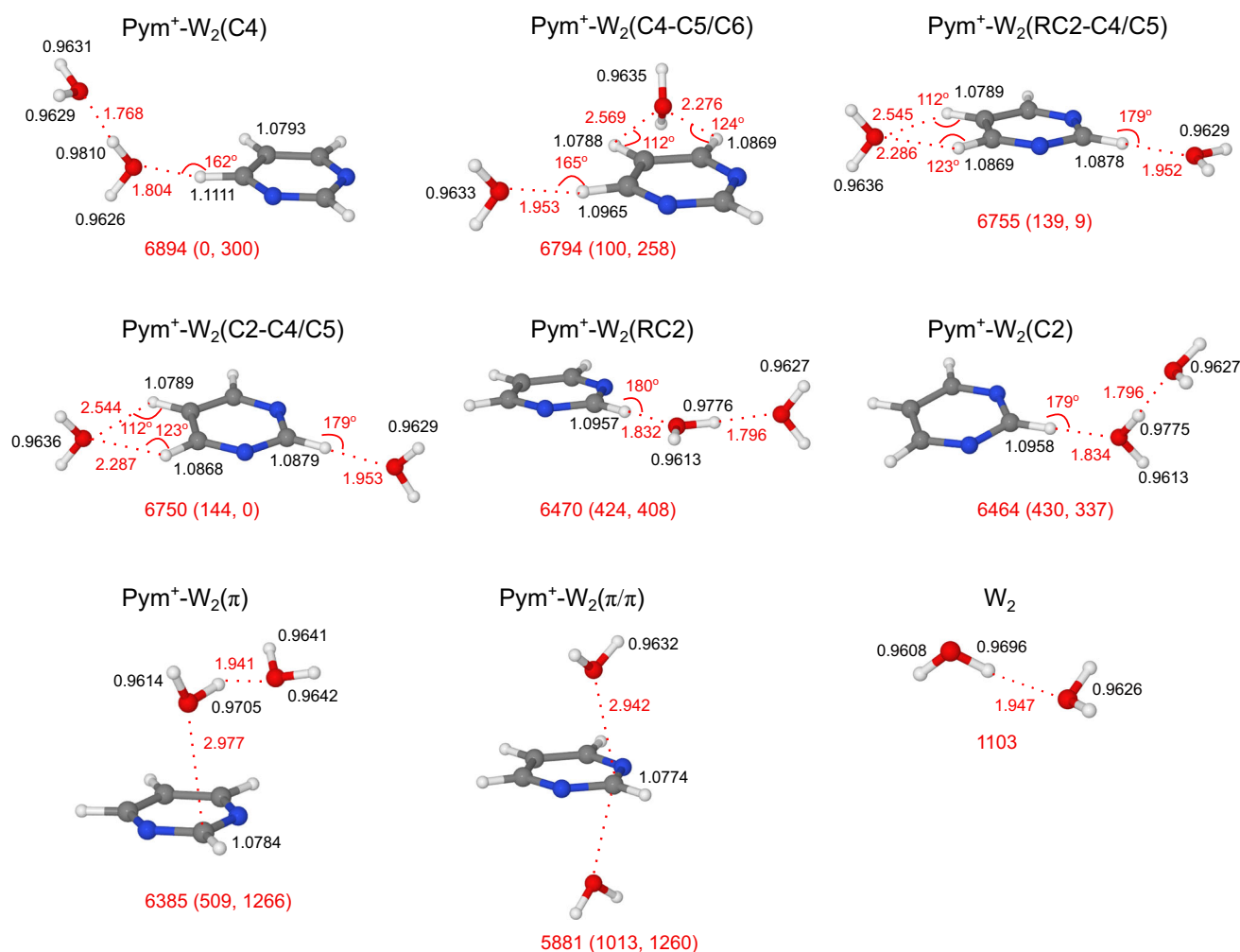
Fig. 6 Optimized structures of various Pym^+-W_2 trimer isomers calculated at the B3LYP-D3/aug-cc-pVTZ level. Binding energies (D_0) and bond lengths are given in cm^{-1} and Å, respectively. Numbers in parentheses correspond to relative energies and free energies in cm^{-1} (E_0, G). For comparison, the structure of W_2 is also provided

168 vs. 190 cm^{-1}). This result is also consistent with the NBO and NCI data ($E^{(2)} = 37.2$ vs. 40 kJ/mol, $-\rho* = 0.026$ vs. 0.027 a.u.) and the reduced charge transfer ($q = 29$ vs. 35 me). On the other hand, the second W solvent perturbs the C5H and C6H proton donors only weakly, which is evident from the longer $R_{CH...O}$ distances ($R_{CH...O} \geqslant 2.2$ Å) and nearly unchanged C–H bond lengths ($r_{CH}\Delta \leqslant 1$ mÅ), resulting in a smaller redshift of the associated ν_{CH} modes ($-\Delta\nu_{C5/6H} \leqslant 20$ cm^{-1}). Unlike the most stable Pym$^+$-W$_2$(C4) trimer, the IR spectrum computed for the C4–C5/C6 isomer features only $\nu_{1/3}$ modes in the free OH stretch range (at 3639/3724 and 3641/3729 cm^{-1}) because of the presence of two single-acceptor W ligands.

For completeness, we also optimized two other isomers of interior ion solvation, in which the second W separately binds to the C2H group either perpendicular or in the plane of the Pym$^+$ ring, denoted C2–C4/C5 and RC2–C4/C5), respectively. In both these

cases, the first W participates in a bifurcated H-bond instead of linear H-bonding, which increases the $R_{CH...O}$ length and lowers the total D_0 value ($D_0 = 6750$ and 6755 cm^{-1}, $E_0 = 144$ and 139 cm^{-1}). The IR spectra computed for these two isomers again feature only $\nu_{1/3}$ modes characteristic of the single-acceptor W ligands. There are two more isomers belonging to the category of exterior ion solvation, RC2 and C2, in which a W$_2$ is attached to C2H. These are relatively high in energy ($E_0 = 424$ and 430 cm^{-1}), because of the low acidity of the C2H group. Their geometric and vibrational properties and cooperative behavior are similar to the related C4 isomer, although the effects are slightly weaker due to the reduced H-bond strengths. Finally, there are two π-bonded isomers belonging to the group of exterior and interior ion solvation, π and π/π, which are very high in energy ($E_0 = 509$ and 1013 cm^{-1}) and also show cooperative and anticooperative effects similar to the H-bonded isomers.

The IRPD spectrum of Pym$^+$-W$_2$ is compared in Fig. 7 (Table 1) to predicted linear IR absorption spec-
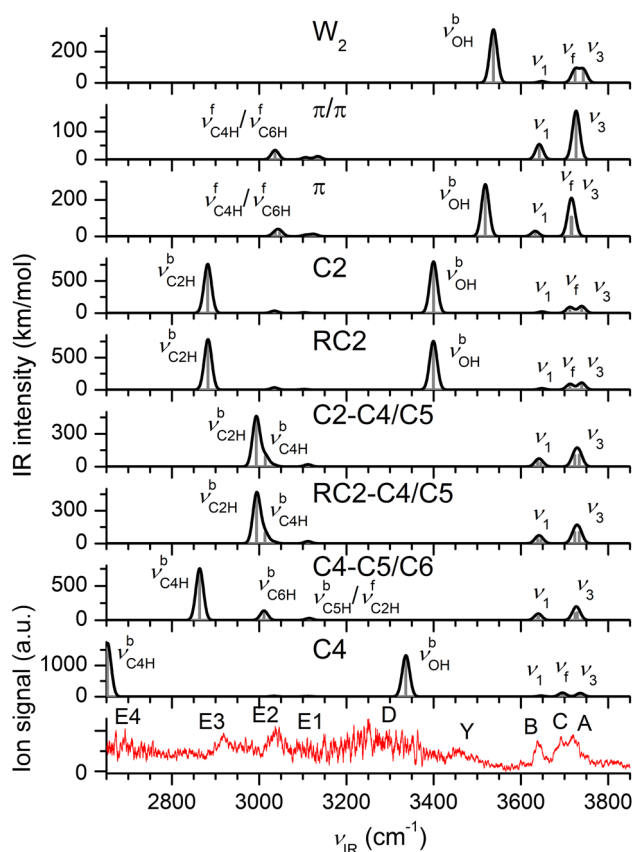
Fig. 7 Comparison of IRPD spectrum of Pym^+-W_2 with linear IR spectra of W_2 and various Pym^+-W_2 isomers (Fig. 6) calculated at the B3LYP-D3/aug-cc-pVTZ level (Table 1)

tra of the optimized Pym^+-W_2 isomers shown in Fig. 6. For convenience, the spectra predicted for W_2 is also included. The experimental $n = 2$ spectrum increases in complexity as compared to the $n = 1$ spectrum. Unlike the dimer spectrum, there are three discernible peaks above $3600\,cm^{-1}$ in the free OH stretch range, namely at 3721 (A), 3637 (B), and $3693\,cm^{-1}$ (C). The IRPD spectrum further exhibits a broad and unresolved feature D peaking at $\sim 3250\,cm^{-1}$ with a width of $200\,cm^{-1}$, together with three sharper transitions Y, E2, and E3 at 3450, 3036, and $2918\,cm^{-1}$, respectively. Moreover, there is broad and unstructured rising signal (E4) toward the beginning of the probed spectral range $(< 2800\,cm^{-1})$, and possibly a weak feature near $3100\,cm^{-1}$ (E1). The new bands C and D are clear spectroscopic signatures for isomers with exterior ion solvation, in which a W_2 dimer is attached to Pym^+. Band C generally arises from a dangling free OH mode of a H-bonded W_2 chain. In the present case, out of the four lowest-energy structures, only the most stable Pym^+-W_2(C4) isomer features such a hydration motif and the computed ν_f mode ($3695\,cm^{-1}$) associated with the single-donor single-acceptor W nicely agrees with this measured $3693\,cm^{-1}$ band. The corresponding bound ν_{OH}^b mode ($3336\,cm^{-1}$) of the same

W ligand corresponds to the broad experimental transition D, and the discrepancy in frequency ($86\,cm^{-1}$) arises mainly because of the strong anharmonicity associated with this H-bonded oscillator. The other two high-frequency bands B and A agree perfectly with the $\nu_{1/3}$ modes ($3646/3736\,cm^{-1}$) of the single-acceptor W. The rising signal at the red end of the scan is assigned to the strongly redshifted ν_{C4H}^b mode predicted at $2652\,cm^{-1}$. Thus, while the C4 global minimum can explain the bands A–C, D, and E4, it cannot readily account for the transitions E1–E3, which may be taken as evidence for the presence of less stable isomers. Indeed, the three other low-energy H-bonded isomers with interior ion solvation and based on the hydration of the two most stable C4 and C4–C5 dimer minima, namely C4–C5/C6, RC2–C4/C5, and C2–C4/C5 with $E_0 = 100$-$144\,cm^{-1}$, can explain bands E1–E3. In this scenario, band E3 at $2918\,cm^{-1}$ is a clear signature for C4–C5/C6 ($\nu_{C4H}^b = 2864\,cm^{-1}$), and the observed blueshift from the $n = 1$ transition is consistent with the predicted shift (18 vs. $22\,cm^{-1}$). We then assign the E2 band to the bound ν_{C6H}^b mode of this isomer calculated at $3011\,cm^{-1}$. To explain the high intensity of band E2, we invoke a significant population of the (R)C2-C4/C5 isomers, which have both very similar predicted IR spectra and relative energies. Bands B and A can account for $\nu_{1/3}$ of the three isomers with interior ion solvation. We may exclude the other two high-energy H-bonded isomers (R)C2 mostly by their high relative energy (although spectroscopically they may contribute). Along a similar line, we may also exclude the two π-bonded isomers for their high energy and the mismatch with the experimental IRPD spectrum. In summary, we assign a predominant population to the most stable Pym^+-W_2(C4) trimer (based on the high intensity of its characteristic bands C and D), along with some contribution of the C4–C5/C6 and (R)C2–C4/C5 isomers.

3.5 Pym^+-W_3

The number of conceivable isomers increases drastically for solvation of Pym^+ with the third W ligand. To this end, we only consider the lowest-energy H-bonded isomers of $n = 3$, which can be derived from the most stable Pym^+-W_2 structures. Their structures and energies are shown in Fig. 8, and their computed IR spectra are compiled in Fig. 9. Further addition of W to the most stable Pym^+-W_2(C4) trimer *via* exterior ion solvation results in either a branched hydration network, Pym^+-W_3(C4-b), or a linear W_3 chain, Pym^+-W_3 (C4-l), which are the lowest energy structures of $n = 3$ with $D_0 = 9965$ and $9893\,cm^{-1}$ ($E_0 = 0$ and $72\,cm^{-1}$). The branched isomer is slightly more stable than the linear one, because the first W ligand is fully solvated and thus all solvent molecules are close to the cation charge. The cooperativity in binding energy of both isomers amounts to 72 and 70%, respectively, and is thus increased compared to the $n = 2$ cluster (47%). As a result, the C4H...O H-bond in $n = 3$ is significantly
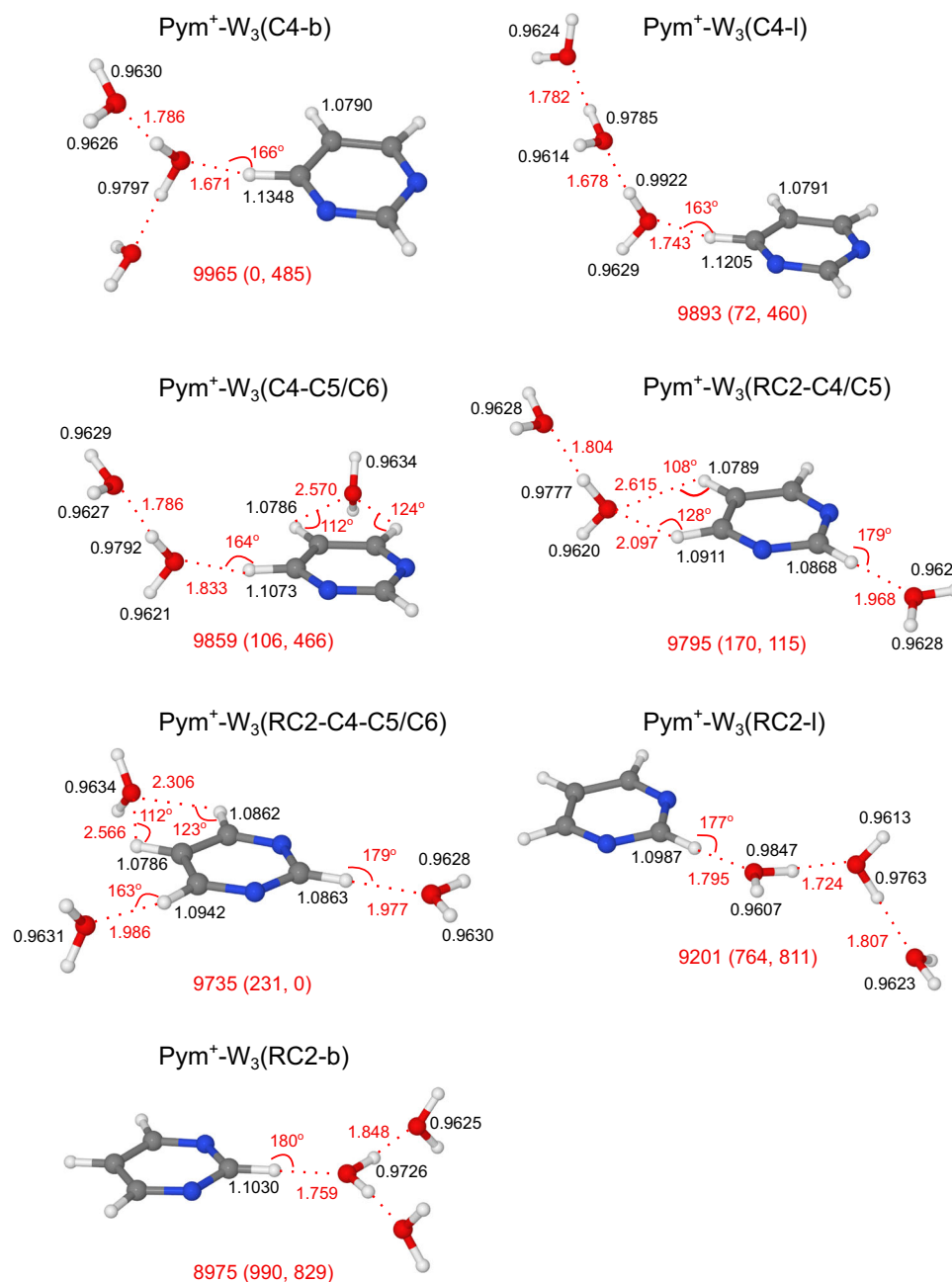
Fig. 8 Optimized structures of various Pym$^+$-W$_3$ isomers calculated at the B3LYP-D3/aug-cc-pVTZ level. Binding energies (D_0) and bond lengths are given in cm^{-1} and Å, respectively. Numbers in parentheses correspond to relative energies and free energies in cm^{-1} (E_0, G)

stronger than in $n = 2$, as observed in the reduced $R_{CH\cdots O}$ bond length ($\Delta R_{CH\cdots O} = -133$ mÅ) and further activated (elongated) C4–H bond ($r_{CH} = 1.1348$ vs. 1.1111 Å). This effect causes a substantial lowering of the $\nu_{C4H}{}^b$ frequency, which is now predicted outside the investigated range at 2316 cm^{-1} with a simultaneous increase in IR intensity ($I_{CH} = 2062$ km/mol). This further enhanced hydration-induced perturbation arises because of the increased PA of W$_3$ as compared to W$_2$ (PA = 862 vs. 808 kJ/mol [87,88]). The NBO and NCI analyses confirm this trend ($E^{(2)} = 105.1$ vs.

65.7 kJ/mol, $-\rho* = 0.055$ vs. 0.038 a.u., $q = 159$ vs. 75 me). Unlike the $n = 2$ case, this branched W$_3$ network lacks the dangling ν_f mode near 3700 cm^{-1} originating from a single-donor W ligand (Fig. 9). Instead, the computed IR spectrum features only $\nu_{1/3}$ modes (3647/3738 cm^{-1}) in the free OH stretch range, resulting from the two terminal single-acceptor W ligands. In addition, the IR spectrum exhibits two redshifted antisymmetric and symmetric $\nu_{OH}{}^b$ modes at 3393 and 3321 cm^{-1}, which originate from the three-coordinated double-donor single-acceptor W ligand. The linear W$_3$
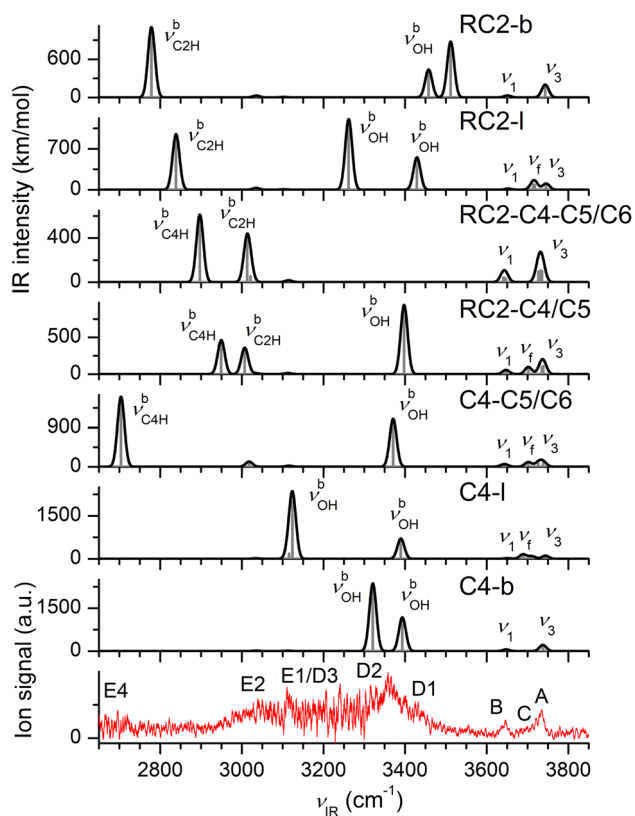
Fig. 9 Comparison of IRPD spectrum of Pym^+-W_3 with linear IR spectra of various Pym^+-W_3 isomers (Fig. 8) calculated at the B3LYP-D3/aug-cc-pVTZ level (Table 1)

chain in the C4-l isomer induces only a slightly weaker perturbation as compared to C4-b, as reflected from the longer CH...O H-bond and the shorter C4–H bond ($R_{CH...O} = 1.743$ vs. 1.671 Å, $r_{CH} = 1.1205$ vs. 1.1348 Å). This is further mirrored in the NBO and NCI data ($E^{(2)} = 82$ vs. 105.1 kJ/mol, $-\rho* = 0.048$ vs. 0.055 a.u., $q = 111$ vs. 159 me). Consequently, the characteristic ν_{C4H}^b mode is slightly less redshifted compared to the C4-b isomer ($-\Delta\nu_{C4H} = 514$ vs. 715 cm^{-1}). However, all these parameters are still higher than for the $n = 2$ case because of the enhanced degree of hydration of the C4H group. Significantly, unlike the branched hydration network, the linear W_3 chain features dangling ν_f modes at 3711 and 3689 cm^{-1} arising from the two single-donor W ligands. The remaining ν_{OH}^b modes associated with these W ligands are calculated at 3390 and 3124 cm^{-1}, which is consistent with their corresponding bond lengths ($r_{OH} = 0.9785$ vs. 0.9922 Å). This difference originates from the different distance of the respective W ligands to the positive charge. Similar to the most stable C4-b/l isomers, the branched and linear W_3 network can develop at the less acidic C2H group, leading to the significantly less stable RC2-b and RC2-l isomers at $E_0 = 990$ and 764 cm^{-1}, respectively. As the geometric, energetic, and spectral properties develop analogous to the C4-b/l isomers, just with reduced magnitude, we discuss them not in detail.

Following the interior ion solvation route, we obtain two further low-energy H-bonded Pym^+-W_3 structures by adding one W solvent to the most stable Pym^+-W_2(C4) trimer at either the C5/C6 or the C2 binding site, namely C4–C5/C6 and RC2–C4/C5, with $D_0 = 9859$ and 9795 cm^{-1} ($E_0 = 106$ and 170 cm^{-1}). These energies correspond to a anticooperative effect of 5.6 and 5.5% upon addition of the third W ligand via interior ion solvation. Finally, we also consider one Pym^+-W_3 isomer of interior ion solvation, in which all three W ligands bind separately to Pym^+ via two single and one bifurcated H-bond (RC2–C4–C5/C6). This isomer is not so high in energy ($E_0 = 231$ cm^{-1}) and becomes lowest in free energy when considering entropy ($G = 0$).

Further hydration of the $n = 2$ cluster strongly affects the IRPD spectrum (Fig. 1). First, the band E3 near 2900 cm^{-1}, which is prominent in the $n = 1$ and 2 spectra disappears for $n = 3$. This band is characteristic for solvation of the C4H group with a single W ligand via an C4H...O H-bond. Hence, this spectral signature can be taken as evidence that in all observed $n = 3$ clusters, the C4H group is solvated at least by two W ligands, as is the case for the three lowest-energy structures in Fig. 8. Second, there is very strong activity in the bound OH stretch range, indicating that clusters with a H-bonded W_2 or W_3 network dominate the $n = 3$ population. This observation excludes significant contributions of $n = 3$ structures in which all three ligands bind separately to the Pym^+ core, i.e., the formation of a H-bonded solvent network is strongly favored over interior ion solvation. Third, the high intensity of band C near 3700 cm^{-1} in the $n = 2$ spectrum drops substantially in the $n = 3$ spectrum, indicating that clusters with single-donor W ligands have only a minor population. Taken all these criteria, the comparison of the IRPD spectrum of Pym^+-W_3 with the IR spectra computed for all isomers in Fig. 9 results in the conclusion of the predominant presence of the most stable C4-b isomer, along with smaller populations of the slightly less stable C4-l and C4–C5/C6 isomers. We can safely exclude the RC2-b/l and RC2–C4/C5 isomers because their intense predicted $\nu_{C2/4H}^b$ transitions are absent in the IRPD spectrum. Similarly, we can exclude the RC2–C4–C5/C6 isomer, which is lowest in free energy, because its intense predicted $\nu_{C2/4H}^b$ transitions are also absent in the IRPD spectrum. Following this interpretation, bands A and B at 3734 and 3646 cm^{-1} are attributed to the $\nu_{3/1}$ modes of C4-b predicted at 3738 and 3647 cm^{-1}, while the features D1 and D2 at 3432 and 3358 cm^{-1} explain the H-bonded ν_{OH}^b modes of the primary W ligand of this isomer computed at 3393 and 3321 cm^{-1}. The strongly redshifted ν_{C4H}^b mode predicted at 2316 cm^{-1} is outside of the scanned range. The other observed bands E1 and E2 at 3110 and 3040 cm^{-1} can be assigned to the free ν_{C2H}^f/ν_{C5H}^f and ν_{C6H}^f modes of this isomer (computed at 3115/3107 and 3035 cm^{-1}), but their predicted relative IR activity cannot account for the high intensity of these IRPD bands. Hence, band D3 at 3110 cm^{-1} (overlapping with band E1) is explained by the ν_{OH}^b mode (3124 cm^{-1})

of the linear C4-l isomer while its second $\nu_{OH}{}^b$ mode calculated at $3390\,\mathrm{cm}^{-1}$ overlaps with the broad feature D2. In addition, this isomer can also account for the weak band C at $3700\,\mathrm{cm}^{-1}$ assigned to its ν_f band computed at $3711/3689\,\mathrm{cm}^{-1}$. While thus essentially all intense features in the IRPD spectrum of $n = 3$ can be rationalized by the two lowest-energy C4-b/l isomers, the weaker E2 and E4 bands may be taken as weak evidence for a minor population of the C4–C5/C6 isomer.

3.6 Further discussion

The present work exploits IRPD spectroscopy and computational chemistry of Pym^+-L_n clusters with L = W and N_2 to determine the preferred solvation motifs as a function of solvent polarity. Quadrupolar and hydrophobic N_2 ligands prefer π stacking above the Pym^+ ring to in-plane $CH\ldots N_2$ H-bonding [47]. The H-bonded isomer contributes only weakly to the IRPD spectrum. In this binding motif, the solvent interacts with the most acidic C4H proton donor group of Pym^+. Because the $N_2\ldots N_2$ interaction is much weaker than the $Pym^+\ldots N_2$ interaction at any binding site, Pym^+-$(N_2)_n$ clusters clearly prefer interior ion solvation [47]. Changing the solvent from N_2 to dipolar, hydrophilic, and protic W has a substantial influence on both the interaction potential and the cluster growth. First, the $Pym^+\ldots W$ interaction is much stronger than the $Pym^+\ldots N_2$ interaction because of the additional charge-dipole forces. Second, W has a stronger preference for formation of H-bonds than N_2 due to its two acidic protons (acting as proton donor) and two nucleophilic lone pairs (acting as proton acceptor). As a result, π complexation is no longer the preferred binding motif and the formation of the $CH\ldots O$ ionic H-bond to most acidic C4H donor group leads to the most stable isomer. Third, because of the strong cooperative three-body effects of H-bonding, Pym^+-W_n clusters clearly prefer exterior to interior ion solvation. However, a minor contribution of isomers corresponding to internal ion solvation is assigned as well. Comparison of Pym^+-W with neutral Pym-W illustrates the effect of the excess positive charge on the intermolecular potential. Neutral Pym-W adopts a coplanar structure with an $OH\ldots N$ H-bond between the OH donor of W and the basic N atom of Pym as acceptor [43,49]. This neutral $OH\ldots N$ H-bond is much weaker and longer ($D_0 = 1790\,\mathrm{cm}^{-1}$, $R_{OH\ldots N} = 1.946\,\text{Å}$) than the $CH\ldots O$ ionic H-bond in Pym^+-W(C4) between the acidic CH proton donor and W, which is stabilized by strong cation-dipole forces ($D_0 = 3597\,\mathrm{cm}^{-1}$, $R_{CH\ldots O} = 1.933\,\text{Å}$). On the other hand, the $CH\ldots O$ ionic H-bond in Pym^+-W(C4) is much weaker than the $NH\ldots O$ ionic H-bond in H^+Pym-W between the much more acidic NH proton donor in N-protonated H^+Pym and W, which is also stabilized by strong cation-dipole forces ($D_0 = 5854\,\mathrm{cm}^{-1}$, $R_{NH\ldots O} = 1.688\,\text{Å}$) [43]. Furthermore, the Pym^--W anion cluster has a slightly weaker and longer $OH\ldots N$ H-bond ($D_0 \sim 5420\,\mathrm{cm}^{-1}$), which is about 0.45 eV ($\sim 3630\,\mathrm{cm}^{-1}$) stronger than

in the neutral because of the additional anion-dipole interaction [89].

Significantly, our IR spectroscopic and computational data on Pym^+-W_n clusters differ in various aspects from the conclusions derived previously from a combined mass spectrometric and computational DFT study at the M06-2X/6-311++G(d,p) level [44]. The M06-2X calculations predict that for Pym^+-W_n with $n = 1$-4 structures with interior ion solvation are more stable than the formation of a H-bonded solvent network [44]. Of course, the mass spectrometric approach was not isomer-sensitive, even though ion mobility was used (due to very low resolution). Our combined IR spectroscopic approach clearly demonstrates that the preferred cluster growth proceeds *via* the formation of a H-bonded solvent network attached to C4H of Pym^+ and not via interior ion solvation. This result is not only clear from the IRPD spectra but also consistent with the E_0 values computed at the B3LYP-D3/aug-cc-pVTZ level. In this sense, the B3LYP-D3 approach is apparently more reliable than the M06-2X level. This is illustrated in more detail for the $n = 1$ cluster. The M06-2X level yields the three minima C4/C5, C2, and C5 with $D_0 = 10.8$, 9.8, and 9.6 kcal/mol (3777, 3428, and $3358\,\mathrm{cm}^{-1}$) [44]. Although there are qualitative similarities in the computed stabilities, there are subtle differences between the two methods. First, the M06-2X work did not report the C4 isomer, which is found most stable in the present B3LYP-D3 calculations and clearly identified by experiment via its characteristic $\nu_{C4H}{}^b$ mode (band E3). Thus, the M06-2X calculations miss the global minimum structure. At this point, we note that the potential between the nearly iso-energetic C4 and C4/C5 isomers is rather flat and it may be easy to miss the C4 isomer in the calculations. Second, the spread in the M06-2X energies of the H-bonded dimers is much larger than for B3LYP-D3 ($\Delta E_0 = 419$ vs. $132\,\mathrm{cm}^{-1}$). Third, the B3LYP-D3 level does not predict a C5 local minimum. Fourth, while the B3LYP-D3 level predicts a clear preference for H-bonding over π stacking (by $\Delta E_0 = 501\,\mathrm{cm}^{-1}$), this question was not addressed in the M06-2X work. In this context, we note that throughout this manuscript, we mostly discussed the E_0 values corresponding to $T = 0\,\mathrm{K}$ and the IRPD spectra correspond mostly to the global minima with $E_0 = 0$. Interestingly, when considering the free energies G calculated at room temperature ($T = 298.15\,\mathrm{K}$), the energetic order changes (Figs. 4, 6, 8). In particular, isomers with linear H-bonds and (nearly) free rotation (in particular at C2H) get lower in energy, and this effect seems beneficial for structures with interior ion solvation. While for $n = 1$, the C4 isomer is most stable at $T = 0$ and 298 K, the global minima on the free energy surface for $n = 2$ and 3 are isomers with interior ion solvation, which are, however, not observed at all in our IRPD spectra. Thus, we conclude that the E_0 data are more appropriate than the G values to predict the isomer population in our supersonic plasma expansion, which may indicate that clusters are significantly colder than room temperature. This view is also consis-

tent with the photofragmentation data. The computed binding energies for the most weakly bound W ligand ($D_0 = 3597$, 3297, and 3071 cm^{-1} for $n = 1$–3) are close to or smaller than the IR photon energy (2650-3800 cm^{-1}), illustrating that single-photon absorption of cold clusters with no or only little energy is sufficient to energetically drive loss of a single W ligand. The experimental enthalpies for W loss of Pym$^+$-W$_n$ derived from ion equilibria measurements in the ~240-290 K range are reported as $-\Delta H = 11.9 \pm 1$, 10.4 ± 1, 9.0 ± 1 kcal/mol for $n = 1$–3 [44]. Although it is unclear, which isomers have been probed in the mass spectrometric experiment at these temperatures, these values are consistent with the enthalpies of the most stable structures predicted by the B3LYP-D3 calculations ($-\Delta H = 10.2$, 9.9, and 9.0 kcal/mol for $n = 1$–3).

In the following, we consider the perturbation of the Pym$^+$ cation by solvation. The N$_2$ ligands preferentially bind to the aromatic ring via π stacking and thus have only a minor impact on the properties of bare Pym$^+$, in particular the C–H bonds and their stretch frequencies. Hence, N$_2$ is a suitable tag for probing the properties of the Pym$^+$ monomer [47]. On the other hand, polar and protic W ligands preferentially form a growing H-bonded W$_n$ network connected to the Pym$^+$ cation via strong and linear CH...O ionic H-bonds to the acidic C4H group. The increasing cooperative force resulting from the monotonically increasing PA of the growing W$_n$ network (PA = 691, 808, 862 kJ/mol for $n = 1$–3) progressively activates the C4–H bond ...[86-88]. This effect is reflected by the increasing C4–H bond length ($r_{CH} = 1.0859 < 1.0981 < 1.1111 < 1.1348$ Å for $n = 0$–3) and the corresponding reduction of the C4–H stretch frequency ($\nu_{C4H} = 3031 > 2842 > 2652 > 2316$ cm^{-1}). These findings are consistent with the NBO and NCI data ($E^{(2)} = 40 < 65.7 < 105.1$ kJ/mol, $-\rho* = 0.027 < 0.038 < 0.055$ a.u. for $n = 1$–3) and the contraction of the CH...O H-bond ($R_{CH...O} = 1.933 > 1.804 > 1.671$ Å). Despite the increasing charge transfer from Pym$^+$ to W$_n$ ($q = 35 < 75 < 159$ me for $n = 1$–3), most of the positive charge resides on the Pym$^+$ cation, because of the large disparity in the ionization energies of Pym and W$_n$ (IE = 9.3 and > 10 eV for Pym and W$_{n<20}$) [64,76,77,90,91]. Furthermore, despite the substantial C–H bond activation, we do not observe any intracluster proton transfer from Pym$^+$ to the W$_n$ solvent cluster in the investigated size range ($n = 1$–3), which is rationalized by the higher solute PA of the pyrimidinyl radical (computed as PA = 869 kJ/mol) as compared to the largest W$_n$ cluster (PA = 862 kJ/mol for $n = 3$). Although the previous mass spectrometric study reports such a solute-to-solvent proton transfer at $n = 4$ in bimolecular reactions [44], consistent with PA = 900 kJ/mol for W$_4$ [88], the spectroscopic proof for such an intracluster proton transfer leading to a C$_3$N$_2$H$_3$-H$^+$W$_4$ structure remains beyond the scope of the present work.

4 Concluding remarks

In summary, the present work combines IR spectroscopy of size-selected Pym$^+$-W$_{1-3}$ clusters in the structure-sensitive CH and OH stretch range with B3LYP-D3 calculations to characterize the microhydration shell around the radical cation of this biomolecular building block. Significantly, the IRPD spectra provide the first reliable experimental information about the binding motifs of Pym$^+$-W$_n$ clusters. In particular, the interpretation of our IR data is in clear conflict with previous conclusions derived from mass spectrometry combined with DFT (M06-2X) calculations [44], illustrating the superior performance of spectroscopy over mass spectrometry concerning structure determination. While the mass-spectrometric report concludes that interior ion solvation is slightly preferred to the formation of a H-bonded solvation network [44], our IRPD spectra clearly show the opposite trend. The salient results may be summarized as follows.

(1) While the aprotic, hydrophobic, nonpolar, or quadrupolar Ar and N$_2$ ligands prefer π stacking to the aromatic Pym$^+$ ring over H-bonding [47,64], the CH...O ionic H-bonds of the protic, hydrophilic, and dipolar W ligands to the slightly acidic CH groups are more stable than π-bonded structures. Because of the additional cation-dipole forces, the Pym$^+$-W interaction is much stronger than the Pym$^+$-N$_2$/Ar bonds. Out of the various possible single and bifurcated CH...O H-bonds, the single and near-linear C4H...O H-bond is most stable, indicating that the C4H group is the most acidic one in Pym$^+$. This Pym$^+$-W(C4) global minimum is slightly more stable than the Pym$^+$-W(C4/C5) local minimum with a bifurcated H-bond, indicating that the potential for W migration around Pym$^+$ is rather flat. While the C4 global minimum is clearly identified by its characteristic IR fingerprint, it was not reported in the previous M06-2X study [44], again illustrating the sensitivity of IR spectroscopy for structure determination. Comparison with neutral Pym-W, H$^+$Pym-W, and Pym$^-$-W illustrates the drastic effect of charge and protonation on the interaction potential with respect to both the equilibrium structure and the interaction strength.

(2) The cluster growth in Pym$^+$-W$_n$ is characterized by the subtle competition between interior ion solvation, where the W ligands bind at multiple binding sites to Pym+, and exterior ion solvation, in which a H-bonded W$_n$ solvent network connects to Pym$^+$ *via* a CH...O H-bond. The IRPD spectra and B3LYP-D3 calculations clearly show that exterior ion solvation, which is strongly cooperative in nature, is preferred to interior ion solvation, which is slightly anticooperative in nature. The strong cooperativity of the formation of the H-bonded network arises from three-body polarization forces of the nearby positive charge. The anticooperativity of interior ion solvation is induced by increased

charge delocalization. Because aprotic hydrophobic ligands, such as L = Ar and N_2, cannot form a strongly bonded solvent network, their clusters grow by interior ion solvation [47,64].

(3) In the most stable Pym^+-W_n structures with a $C4H\ldots W_n$ H-bond, the W_n cluster progressively activates the most acidic C4–H bond of Pym^+ as n increases from 1 to 3, resulting in an increasing elongation of the C4–H bond, a contraction of the $C4H\ldots O$ H-bond, and increasing charge transfer from Pym^+ to W_n. However, we do not observe any solute-to-solvent proton transfer, which is consistent with the higher PA values of the pyrimidinyl radical as compared to W_{1-3}. Nonetheless, both the mass spectrometric experiments [44] and the PA values of W_n suggest that such an intracluster proton transfer may occur at $n \geqslant 4$. To this end, spectroscopic interrogation of larger hydrated clusters is required to probe this proton migration, which is an important biophysical phenomenon.

Author contributions

KC performed the experiment and calculations. KC and OD analyzed the data and wrote the paper. OD coordinated the project.

Data Availability Statement This manuscript has data included as electronic supplementary material.

References

1. P.B. Dervan, Biorg. Med. Chem. **9**, 2215 (2001)
2. B. Bagchi, Chem. Rev. **105**, 3197 (2005)
3. P. Ball, Chem. Rev. **108**, 74 (2008)
4. M. Chaplin, Nat. Rev. Mol. Cell Biol. **7**, 861 (2006)
5. M. Feig, B.M. Pettitt, Biopolymers **48**, 199 (1998)
6. Y. Levy, J.N. Onuchic, Annu. Rev. Biophys. Biomol. Struct. **35**, 389 (2006)
7. C. Mattos, Trends Biochem. Sci. **27**, 203 (2002)
8. S.K. Pal, A.H. Zewail, Chem. Rev. **104**, 2099 (2004)
9. B. Schneider, D. Cohen, H.M. Berman, Biopolymers **32**, 725 (1992)
10. D. Zhong, S.K. Pal, A.H. Zewail, Chem. Phys. Lett. **503**, 1 (2011)
11. C.L. Perrin, J.B. Nielson, Annu. Rev. Phys. Chem. **48**, 511 (1997)
12. B. Giese, S. Wessely, Chem. Commun. Z. Phys. Chem.
13. M.R.A. Blomberg, P.E.M. Siegbahn, Biochim. Biophys. Acta **1757**, 969 (2006)
14. H. Ishikita, K. Saito, J.R. Soc, Interface **11**, 20130518 (2014)
15. B. Nguyen, S. Neidle, W.D. Wilson, Acc. Chem. Res. **42**, 11 (2009)
16. S.K. Pal, L. Zhao, A.H. Zewail, PNAS **100**, 8113 (2003)
17. T.V. Chalikian, G.E. Plum, A.P. Sarvazyan, K.J. Breslauer, Biochemistry **33**, 8629 (1994)
18. J.-P. Schermann, *Spectroscopy and Modeling of Biomolecular Building Blocks* (Elsevier Science, Amsterdam, 2008)
19. O. Dopfer, Z. Phys. Chem. **219**, 125 (2005)
20. M.S. de Vries, P. Hobza, Annu. Rev. Phys. Chem. **58**, 585 (2007)
21. P. Hobza, K.M. Dethlefs, *Non-Covalent Interactions: Theory and Experiment* (Royal Society of Chemistry Cambridge, UK, 2009)
22. A. Kamariotis, O.V. Boyarkin, S.R. Mercier, R.D. Beck, M.F. Bush, E.R. Williams, T.R. Rizzo, J. Am. Chem. Soc. **128**, 905 (2006)
23. M.F. Bush, J.S. Prell, R.J. Saykally, E.R. Williams, J. Am. Chem. Soc. **129**, 13544 (2007)
24. T.M. Chang, J.S. Prell, E.R. Warrick, E.R. Williams, J. Am. Chem. Soc. **134**, 15805 (2012)
25. N.C. Polfer, J. Oomens, Mass Spectrom. Rev. **28**, 468 (2009)
26. J.M. Bakker, R.K. Sinha, T. Besson, M. Brugnara, P. Tosi, J.-Y. Salpin, P. Maître, J. Phys. Chem. A **112**, 12393 (2008)
27. M. Miyazaki, A. Fujii, T. Ebata, N. Mikami, J. Phys. Chem. A **108**, 10656 (2004)
28. J.M. Lisy, J. Chem. Phys. **125**, 132302 (2006)
29. A.M. Rijs, J. Oomens, *Gas-Phase IR Spectroscopy and Structure of Biological Molecules* (Springer, Berlin, 2015)
30. O. Dopfer, M. Fujii, Chem. Rev. **116**, 5432 (2016)
31. K. Chatterjee, O. Dopfer, Chem. Sci. **9**, 2301 (2018)
32. K. Chatterjee, Y. Matsumoto, O. Dopfer, Angew. Chem. Int. Ed. **58**, 3351 (2019)
33. K. Chatterjee, O. Dopfer, Phys. Chem. Chem. Phys. **21**, 25226 (2019)
34. K. Chatterjee, O. Dopfer, J. Phys. Chem. A **124**, 1134 (2020)

35. W. Saegner, *Principles of Nucleic Acid Structure* (Springer, New York, 1984)
36. K. Wei, E. Karen, W. Joanne, Curr. Drug Metab. **5**, 63 (2004)
37. M. Nuevo, S.N. Milam, S.A. Sandford, J.E. Elsila, J.P. Dworkin, Astrobiology **9**, 683 (2009)
38. P.P. Bera, M. Nuevo, S.N. Milam, S.A. Sandford, T.J. Lee, J. Chem. Phys. **133**, 104303 (2010)
39. E. Mendoza, G.C. Almeida, D.P.P. Andrade, H. Luna, W. Wolff, M.L.M. Rocco, H.M. Boechat-Roberty, Mon. Not. R. Astron. Soc. **433**, 3440 (2013)
40. P.G. Stoks, A.W. Schwartz, Nature **282**, 709 (1979)
41. P.G. Stoks, A.W. Schwartz, Geochim. Cosmochim. Acta **45**, 563 (1981)
42. M.P. Callahan, K.E. Smith, H.J. Cleaves, J. Ruzicka, J.C. Stern, D.P. Glavin, C.H. House, J.P. Dworkin, PNAS **108**, 13995 (2011)
43. K. Chatterjee, O. Dopfer, Phys. Chem. Chem. Phys. **22**, 13092 (2020)
44. A.M. Hamid, P. Sharma, M.S. El-Shall, R. Hilal, S. Elroby, S.G. Aziz, A.O. Alyoubi, J. Chem. Phys. **139**, 084304 (2013)
45. I.K. Attah, S.P. Platt, M. Meot-Ner, M.S. El-Shall, S.G. Aziz, A.O. Alyoubi, Chem. Phys. Lett. **613**, 45 (2014)
46. K. Chatterjee, O. Dopfer, Phys. Chem. Chem. Phys. **19**, 32262 (2017)
47. K. Chatterjee, O. Dopfer, Phys. Chem. Chem. Phys. **22**, 17275 (2020)
48. B. Zhang, Y. Cai, X. Mu, N. Lou, X. Wang, J. Chem. Phys. **117**, 3701 (2002)
49. S. Melandri, M.E. Sanz, W. Caminati, P.G. Favero, Z. Kisiel, J. Am. Chem. Soc. **120**, 11504 (1998)
50. A. Destexhe, J. Smets, L. Adamowicz, G. Maes, J. Phys. Chem. **98**, 1506 (1994)
51. X. Huang, J.-P. Aranguren, J. Ehrmaier, J.A. Noble, W. Xie, A.L. Sobolewski, C. Dedonder-Lardeux, C. Jouvet, W. Domcke, Phys. Chem. Chem. Phys. **22**, 12502 (2020)
52. O. Dopfer, Int. Rev. Phys. Chem. **22**, 437 (2003)
53. M.J. Frisch et al., *Gaussian 09, Version D.01* (Gaussian Inc, Wallingford, CT, 2009)
54. K. Chatterjee, O. Dopfer, Phys. Chem. Chem. Phys. **21**, 15157 (2019)
55. K. Chatterjee, O. Dopfer, J. Chem. Phys. **149**, 174315 (2018)
56. K. Chatterjee, O. Dopfer, J. Phys. Chem. A. **123**, 7637 (2019)
57. K. Chatterjee, O. Dopfer, Astrophys. J. **865**, 114 (2018)
58. J. Klyne, O. Dopfer, Phys. Chem. Chem. Phys. **21**, 2706 (2019)
59. J. Klyne, M. Miyazaki, M. Fujii, O. Dopfer, Phys. Chem. Chem. Phys. **20**, 3092 (2018)
60. M. Schütz, Y. Matsumoto, A. Bouchet, M. Öztürk, O. Dopfer, Phys. Chem. Chem. Phys. **19**, 3970 (2017)
61. B.E. Rocher-Casterline, L.C. Ch'ng, A.K. Mollner, H. Reisler, J. Chem. Phys. **134**, 211101 (2011)
62. L. Bokobza-Sebagh, J. Zarembowitch, Spectrochim. Acta A **32**, 797 (1976)
63. K.K. Innes, I.G. Ross, W.R. Moomaw, J. Mol. Spectrosc. **132**, 492 (1988)
64. S.-I. Sato, K. Omiya, K. Kimura, J. Electron. Spectrosc. Relat. Phenom. **97**, 121 (1998)
65. G. Herzberg, *Molecular Spectra and Molecular Structure. II. Infrared and Raman Spectra of Polyatomic Molecules* (Krieger Publishing Company Malabar, FL, 1991)
66. A.E. Reed, L.A. Curtiss, F. Weinhold, Chem. Rev. **88**, 899 (1988)
67. E.R. Johnson, S. Keinan, P. Mori-Sánchez, J. Contreras-García, A.J. Cohen, W. Yang, J. Am. Chem. Soc. **132**, 6498 (2010)
68. J. Contreras-García, E.R. Johnson, S. Keinan, R. Chaudret, J.-P. Piquemal, D.N. Beratan, W. Yang, J. Chem. Theory Comput. **7**, 625 (2011)
69. L. Fernholt, C. Romming, Acta Chem. Scand. **32**, 271 (1978)
70. S. Albert, M. Quack, J. Mol. Spectrosc. **243**, 280 (2007)
71. S. Breda, I.D. Reva, L. Lapinski, M.J. Nowak, R. Fausto, J. Mol. Struct. **786**, 193 (2006)
72. R.C. Lord, A.L. Marston, F.A. Miller, Spectrochim. Acta. **9**, 113 (1957)
73. Z.N. Heim, B.K. Amberger, B.J. Esselman, J.F. Stanton, R.C. Woods, R.J. McMahon, J. Chem. Phys. **152**, 104303 (2020)
74. R. Gleiter, E. Heilbronner, V. Hornung, Helv. Chim. Acta. **55**, 255 (1972)
75. A.W. Potts, D.M.P. Holland, A.B. Trofimov, J. Schirmer, L. Karlsson, K. Siegbahn, J. Phys. B **36**, 3129 (2003)
76. J.H. Kim, J.H. Lee, H. Hwang, H.L. Kim, C.H. Kwon, Phys. Chem. Chem. Phys. **16**, 1590 (2014)
77. M. Riese, J. Grotemeyer, Anal. Bioanal. Chem. **386**, 59 (2006)
78. A.G. Császár, G. Czakó, T. Furtenbacher, J. Tennyson, V. Szalay, S.V. Shirin, N.F. Zobov, O.L. Polyansky, J. Chem. Phys. **122**, 214305 (2005)
79. N. Solcà, O. Dopfer, Chem. Phys. Lett. **347**, 59 (2001)
80. M. Miyazaki, A. Fujii, N. Mikami, J. Phys. Chem. A **108**, 8269 (2004)
81. K. Kleinermanns, C. Janzen, D. Spangenberg, M. Gerhards, J. Phys. Chem. A **103**, 5232 (1999)
82. T. Sawamura, A. Fujii, S. Sato, T. Ebata, N. Mikami, J. Phys. Chem. **100**, 8131 (1996)
83. C. Unterberg, A. Jansen, M. Gerhards, J. Chem. Phys. **113**, 7945 (2000)
84. N. Solcà, O. Dopfer, J. Phys. Chem. A **107**, 4046 (2003)
85. N. Solcà, O. Dopfer, Chem. Phys. Lett. **325**, 354 (2000)
86. E.P.L. Hunter, S.G. Lias, J. Phys. Chem. Ref. Data. **27**, 413 (1998)
87. D.J. Goebbert, P.G. Wenthold, Eur. J. Mass Spectrom. **10**, 837 (2004)
88. A. Courty, M. Mons, J. Le Calvé, F. Piuzzi, I. Dimicoli, J. Phys. Chem. A **101**, 1445 (1997)
89. J.T. Kelly, S. Xu, J. Graham, J.M. Nilles, D. Radisic, A.M. Buonaugurio, K.H. Bowen, N.I. Hammer, G.S. Tschumper, J. Phys. Chem. A **118**, 11901 (2014)
90. L. Belau, K.R. Wilson, S.R. Leone, M. Ahmed, J. Phys. Chem. A **111**, 10075 (2007)
91. S. Tomoda, K. Kimura, Chem. Phys. Lett. **102**, 560 (1983)
92. Z.S. Huang, R.E. Miller, J. Chem. Phys. **91**, 6613 (1989)
93. F. Huisken, M. Kaloudis, A. Kulcke, J. Chem. Phys. **104**, 17 (1996)
94. K. Kuyanov-Prozument, M.Y. Choi, A.F. Vilesov, J. Chem. Phys. **132**, 014304 (2010)